



**HAL**  
open science

## Synthesis of the Elusive Doublewall Nanotubes and Nanocones(Horns) of MoS<sub>2</sub> via Focused Solar Ablation

Timothée Barbe, Rita Rosentsveig, Olga Brontvein, M.B. Sreedhara, Kai Zheng, Françoise Bataille, Alexis Vossier, Gilles Flamant, Ivano Castelli, Jeffrey Gordon, et al.

### ► To cite this version:

Timothée Barbe, Rita Rosentsveig, Olga Brontvein, M.B. Sreedhara, Kai Zheng, et al.. Synthesis of the Elusive Doublewall Nanotubes and Nanocones(Horns) of MoS<sub>2</sub> via Focused Solar Ablation. *Advanced Materials Interfaces*, In press, pp.2201930. 10.1002/admi.202201930 . hal-03863268

**HAL Id: hal-03863268**

**<https://hal.science/hal-03863268>**

Submitted on 21 Nov 2022

**HAL** is a multi-disciplinary open access archive for the deposit and dissemination of scientific research documents, whether they are published or not. The documents may come from teaching and research institutions in France or abroad, or from public or private research centers.

L'archive ouverte pluridisciplinaire **HAL**, est destinée au dépôt et à la diffusion de documents scientifiques de niveau recherche, publiés ou non, émanant des établissements d'enseignement et de recherche français ou étrangers, des laboratoires publics ou privés.

**Synthesis of the elusive doublewall nanotubes and nanocones(horns) of MoS<sub>2</sub> via focused solar ablation**

*Timothée Barbe, Rita Rosentsveig, Olga Brontvein, M.B. Sreedhara, Kai Zheng, Françoise Bataille, Alexis Vossier, Gilles Flamant\*, Ivano E. Castelli, Jeffrey M. Gordon\* and Reshef Tenne\**

Timothée Barbe, Françoise Bataille, Alexis Vossier, Gilles Flamant  
PROMES-CNRS, Processes, Materials and Solar Energy Laboratory, 7 rue du Four solaire,  
66120 Font Romeu-Odeillo, France  
E-mail: gilles.flamant@promes.cnrs.fr

Rita Rosentsveig, M.B. Sreedhara, Reshef Tenne  
Department of Molecular Chemistry and Materials Science, Weizmann Institute of Science,  
Rehovot 7610001, Israel  
E-mail: reshef.tenne@weizmann.ac.il

Olga Brontvein  
Department of Chemical Research Support, Weizmann Institute of Science, Rehovot  
7610001, Israel

Kai Zheng, Ivano E. Castelli  
Department of Energy Conversion and Storage, Technical University of Denmark, DK-2800  
Kgs. Lyngby, Denmark

Timothée Barbe, Françoise Bataille  
Université de Perpignan Via Domitia (UPVD), 52 Avenue Paul Alduy, 66100, Perpignan,  
France

Jeffrey M. Gordon  
Department of Solar Energy and Environmental Physics, Jacob Blaustein Institutes for Desert  
Research, Ben-Gurion University of the Negev, Sede Boqer Campus 8499000, Israel  
E-mail: jeff@bgu.ac.il

Keywords: MoS<sub>2</sub>, nanotubes, nanocones, nanohorns, solar ablation, solar furnace

The synthesis of fundamentally small MoS<sub>2</sub> nanotubes and nanocones(horns) that have proven elusive in prior studies has been achieved via ablation of a precursor mixture of crystallites of MoS<sub>2</sub>+MoO<sub>3</sub> by highly concentrated solar radiation. The special far-from-equilibrium conditions achieved in our solar furnace proved conducive to the generation of these singular nanostructures. Extensive electron microscopy and characterization results (TEM, ED, SAED, XRD, STEM-EDS and HAADF) reveal a range of nanoparticle shapes and sizes based on which reaction mechanisms are proposed. Molecular dynamics simulations indicate that the sizable thermal fluctuations intrinsically produced in the high-temperature solar reactor soften the MoS<sub>2</sub> nanostructures, yielding corrugated layers that favor nanostructures with only a few layers, in agreement with the experimental observations.

## 1. Introduction

Despite extensive theoretical predictions and computations of doublewall MoS<sub>2</sub> nanotubes and nanoscrolls - nanostructures near the fundamental smallness limit for this layered compound, of both basic and applied interest - their experimental realization has proven tenuous. A successful method for the reproducible syntheses of an assortment of these nanoparticles is reported here, based on the ablation of MoS<sub>2</sub> jointly with MoO<sub>3</sub> powder with highly concentrated sunlight.<sup>1</sup> Most notable is the generation of doublewall MoS<sub>2</sub> nanotubes <10 nm in diameter and a few hundred nm in length, along with a variety of ~20 nm MoS<sub>2</sub> nanoscrolls (cones and horns).

Such doublewall nanotubes could not be obtained in previous investigations that employed close-to-equilibrium reactions at temperatures <1000°C. But they were successfully generated at the far-from-equilibrium conditions created in our solar furnace (**Fig. 1**). The key caveats, however, are that their yields were small, and the process was random rather than well controlled, as elaborated below. The structural characteristics of the distinctive nanostructures presented here are assessed from a wide range of electron microscopy and material characterization measurements, based on which growth mechanisms are proposed.

Numerous research and review articles have documented the synthesis, characterization and applications of comparably small nanoparticles from other 2D layered materials that subsume

(but are not limited to) graphite, WS<sub>2</sub> and BN. They have scrutinized the structural, chemical and synthetic-pathway similarities and distinct dissimilarities to MoS<sub>2</sub>. Because the focus of this paper is the experimental realization, characterization and understanding specifically of singular MoS<sub>2</sub> nanotubes and nanoscrolls, and in the spirit of economy of presentation, a reexamination of these comparisons is not pursued here. Rather, only observations directly and explicitly related to MoS<sub>2</sub> nanostructures which can place our results in better perspective are briefly reviewed in the remainder of this section.

In terms of previous syntheses, MoS<sub>2</sub> nanoscrolls were first prepared *via* heating amorphous MoS<sub>x</sub> at 400°C for a few hours.<sup>2</sup> Multiwall WS<sub>2</sub><sup>3</sup> and MoS<sub>2</sub><sup>4</sup> nanotubes were obtained by the reaction of their respective MO<sub>3</sub> (M = Mo and W) nanoparticles in H<sub>2</sub>S under a mildly reducing atmosphere at 800-1000°C. While single and doublewall nanotubes of carbon<sup>5,6</sup> and boron nitride (BN)<sup>7</sup> (from their respective layered 2D crystals) were readily obtained as a pure phase, comparably small nanotubes of MoS<sub>2</sub> and WS<sub>2</sub> were rarely reported<sup>8,9</sup>. This was attributed to the large bending energy of the triple S-M-S layers, which is about 10 times larger than that of the graphitic or BN layer.<sup>10</sup> It poses a major challenge to identify experimental procedures for the repeatable synthesis of these nanoparticles in quantities sufficient for conclusive characterization. Chemical vapor deposition (CVD) of single layer, up to a few layers, of MoS<sub>2</sub> at <800°C on different substrates was adopted to grow triangular crystallites that expand laterally and grow until full coverage is attained.<sup>11-13</sup> In the present experiments, such triangular MoS<sub>2</sub> crystallites made of a few layers were often observed, along with two edges folding to form nanoscrolls a few layers thick.

For the formation mechanism of the nanohorns(cones) produced in our solar ablation experiments, softening of the MoS<sub>2</sub> layers at the high temperatures produced in solar ablation can be conducive to scrolling. This in turn favors the scrolling of the triangular edges. Furthermore, few-wall nanohorns were also frequently observed, akin both in structure and formation pathway to carbon nanohorns.<sup>14</sup>

Arc-discharge<sup>15</sup> and laser ablation<sup>16</sup> of 2D materials provide highly exergonic conditions, which are congruent with the far-from-equilibrium growth of nanostructures with minimal diameters, comprising only a few layers. Laser ablation<sup>17,18</sup> - and subsequently solar ablation<sup>19</sup> - of MoS<sub>2</sub> powder provided the first evidence for fundamentally small MoS<sub>2</sub> nanooctahedra with diameters <3 nm, composed of 2-3 layers only. Intricate nanostructures made of MoS<sub>2</sub>

nanooctahedra coated conformably by a few quasi-spherical MoS<sub>2</sub> layers were obtained by irradiating MoS<sub>2</sub> with a focused solar beam, but only with sparse yields and problematical repeatability.<sup>19</sup>

Thermodynamic modeling of MoS<sub>2</sub> nano-onions predicted an elaborate stability hierarchy that was found to be consistent with the experimental observations. Indeed the nanooctahedra are stable for the smallest radii and up to about eight MoS<sub>2</sub> layers (~10 nm radius). Beyond that size, faceted polyhedral nanoparticles become more stable, until the macroscopic limit is reached (at a diameter of ca. 200 nm), at which point MoS<sub>2</sub> flakes become the most stable structures.

A lesson learned from these highly energetic syntheses was that invariably the process could not be well controlled and the yields of the minimum-size hollow closed nanoparticles were low. This turns out to be true for solar ablation as well. The random nature of the generation of these nanostructures is reflected in the large dispersion in their size, type and number of layers (Table S1 in the Supporting Information, SI), with standard deviations exceeding 50% of average values, based on TEM images. A challenge for future programs would be finding experimental conditions that allow controlled syntheses.

To evaluate the nature of the high temperature growth of these nanostructures, we conducted detailed molecular dynamics simulations (Section 4). These calculations show that substantial thermal fluctuations (of the type intrinsic to the solar reactor) can soften the MoS<sub>2</sub> nanostructures, leading to nanoparticles with only a few corrugated layers. Although these computations suggest how large fluctuations and the resulting corrugation of molecular layers may account for the preponderance of nanostructures with no more than only a few layers in the experimental results, they are insufficient to contribute toward formulating the nanoparticle formation mechanisms depicted below.

Section 2 reports experimental details along with comprehensive electron microscopy and material characterization results. Section 3 provides an in-depth analysis of the variety of MoS<sub>2</sub> nanostructures synthesized, including their shape, size and frequency of occurrence. Section 4 focuses on the molecular dynamics simulations and their predictions vis-a-vis the experimental results. Section 5 offers some conclusions with an eye toward future experiments.

## 2. Experimental

### 2.1. Synthesis

**Figure 1a** shows a schematic of the solar facility used to ablate a mixture of MoO<sub>3</sub> (Alfa Aesar, 99.95% pure) and MoS<sub>2</sub> (Sigma Aldrich, 98% pure) powders. The outdoor solar tracking heliostat reflects the beam radiation to an indoor static paraboloidal dish 1.5 m in diameter that concentrates it onto the focal zone (12 mm diameter disk). The solar flux concentration achieved in the maximum-irradiance core region of the focal spot at solar noon under clear-sky conditions is 10,000 suns (1 sun = 1 kW/m<sup>2</sup>). Prior to irradiation, the reactor is flushed with argon for half an hour to ensure an inert inner atmosphere is maintained at ambient pressure (1 bar) during the reaction. Highly concentrated sunlight rapidly vaporizes the solid precursor (mixed MoS<sub>2</sub> and MoO<sub>3</sub> powders in different proportions) into a continuous jet-flow,<sup>1</sup> spreading it within the reactor (**Fig. 1b-c**). The vaporized species nucleate and grow as they experience a gradual decrease in temperature during their time of flight. Nanoparticle formation then ensues, followed by quenching and deposition on the components of the condensation zones (**Fig. 1a**), namely, the cold finger, the Pyrex wall and the nanoparticle filter.

The temperature in the reactor is mainly determined by the vaporization temperature of the solid precursor (>1500 K at 1 bar). It can be reduced by modulating the blade shutters between the heliostat and the paraboloidal dish concentrator (**Fig. 1a**). The temperature distribution inside the reactor was previously simulated by computational fluid dynamics software and validated against experimental measurements.<sup>1</sup> Both the model and the measurements confirmed that the temperature of the jet of the vaporized species generated during solar ablation is close to the precursor's vaporization temperature. This supports the proposition that the formation of the nanoparticles in the solar furnace occurs at a noticeably higher temperature than in conventional VGS methods ( $\leq 900^\circ\text{C}$ ). It also reinforces the explanation that the high reactor temperature and the kinetic barrier favor the production of doublewall nanotubes (*vide infra*).

**Figure S1** in the SI shows the calculated temperature profile in the reactor (at ambient pressure)<sup>1</sup>, with the hottest spot (1500 K) at the center of the upper surface of the precursor powder on which the solar beam is focused. The temperature on the inner walls of the reactor and on the cold finger is around 400 K. These figures would indicate that the temperature in

the hot reaction zone should lie between the vaporization temperatures of sulfur (720 K) and MoS<sub>2</sub> (~2000 K) at ambient pressure. It is there that the nanoparticles form, grow and mature by sulfurization of the suboxide nanoparticles into sulfide nanoparticles, which is expanded upon in Section 2B.

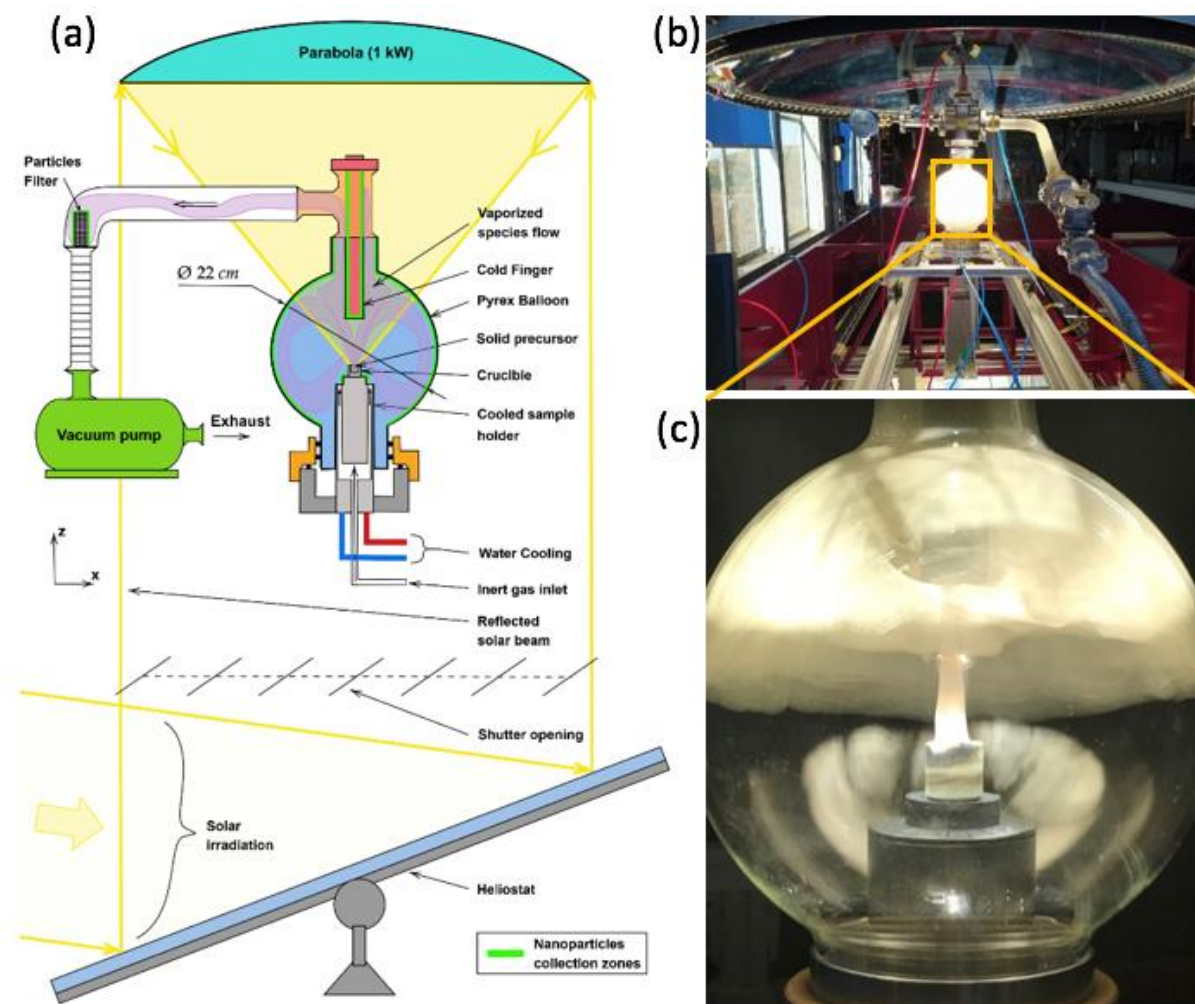


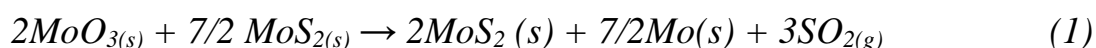
**Figure 1.** The solar furnace used for ablation by highly concentrated sunlight. (a) Schematic rendering with labelling of each component. (b) Snapshot of the reactor during solar ablation. (c) Photo of the reactor during a flow-visualization experiment, showing the heated crucible, plumes from an ablated precursor powder, and the cold finger on which products condense (**Figs. 1a** and **1c** adopted from Ref. 1).

## 2.2. Collection of the product

Once irradiation was terminated and the reactor was opened, a brush was used with ethanol to scratch the walls and the cold finger in order to collect the product powder consisting of large lumps of ablated material that were difficult to break into small enough pieces for a proper

transmission electron microscopy (TEM) analysis. Therefore, in ensuing experiments, the product was first ground mechanically before sonication (10 min) in ethanol. Samples for TEM analysis were collected also by sonicating the metallic filter in ethanol for 10 min. Subsequently, the suspension was dripped onto a TEM grid, using a Pasteur pipette, and the grid was blotted and dried toward preparing it for the electron microscopy analysis. It should also be noted that up to 80% (by weight) of the vaporized species was trapped in the nanoparticle filter, and most of the TEM images correspond to powders extracted from that filter.

The decomposition of MoO<sub>3</sub> at elevated temperatures has been investigated thoroughly,<sup>20</sup> based on which the synthesis pathway to MoS<sub>2</sub> nanostructures is believed to be:



Accordingly, a key element of the proposed nanoparticle formation mechanism is that incongruent high-temperature evaporation of the MoS<sub>2</sub> powder leads to its decomposition. The sulfur vapor thereby generated reacts with the oxide vapors, and the products condense into the observed assortment of nanostructures as well as into MoS<sub>2</sub> flakes and elemental Mo. The latter was visibly evident in every experiment as a pellet of pure Mo that adhered to the bottom of the crucible holding the precursor powder. An alternative possible chemical route is the high-temperature (>1000°C) reduction of the vaporized MoO<sub>3</sub> into MoO<sub>2</sub> + 1/2 O<sub>2</sub> and, to a far lesser extent, Mo<sub>4</sub>O<sub>11</sub> nanowhiskers + 1/2 O<sub>2</sub>.<sup>20,21</sup> These molybdenum suboxide nanowhiskers react vigorously with sulfur vapor, converting it to MoS<sub>2</sub> nanotubes.<sup>22</sup> This growth mechanism of the nanostructures resembles a previous one, whereby MoS<sub>2</sub> powder was solar ablated jointly with lead nanoparticles.<sup>23</sup> With the help of the lead catalyst, the ablated vapor condensed into MoO<sub>3-x</sub> nanowhiskers, which were sulfurized *in-situ* leading to multiwall MoS<sub>2</sub> nanotubes.

### 2.3. Characterization

Given the small sizes of the reported nanostructures and their scarcity, TEM was the main tool used for the characterization of the ablation products, which was encumbered by the nanostructures always being attached to bulky MoS<sub>2</sub> flakes. In this study, we did not succeed in separating them sufficiently for separate characterization. Such a separation should, however, be possible by adding a filtration step to the procedure of retrieving the products and preparing them for TEM - intended for future experiments.

#### **2.4. X-ray diffraction (XRD) analysis**

X-ray powder diffraction was performed using a TTRAX III (Rigaku, Tokyo, Japan) theta-theta diffractometer equipped with a rotating copper anode X-ray tube operating at 50 kV/200 mA. The samples were prepared on a zero-background Si substrate. They were scanned using the Cu K $\alpha$  line in specular diffraction mode ( $\theta/2\theta$  scans) from 4-90° ( $2\theta$ ) with a step size of 0.02° and a scan rate of 0.5° per min.

#### **2.5. Scanning electron microscopy (SEM) analysis and Energy dispersive X-ray spectroscopy (EDS)**

A Zeiss Sigma 500 model was used for the scanning electron microscopy (SEM) analysis. A minute quantity of native sample was dispersed on carbon tape. Energy dispersive X-ray spectroscopy (EDS) analysis was performed using a Bruker QUANTAX FlatQUAD retractable detector.

#### **2.6. TEM analysis**

High resolution electron microscopy analysis was found to be difficult due to the rarity of the species. This situation was further exacerbated because the investigated nanostructures were always attached to relatively thick MoS<sub>2</sub> flakes and other ablation products. A Talos F200X G2 TEM 200 kV (Thermo Fisher Scientific, USA) scanning TEM (STEM) was used for most of the rudimentary analysis. The TEM images, including intensity profiles along the *c*-axis and selected area electron diffraction (SAED), were analyzed with Velox, Digital Micrograph 3.4.0 (Gatan) and ImageJ softwares. Energy dispersive X-ray analysis (STEM-EDS) was used for the chemical analysis of the products. High angle annular dark field (HAADF) analysis in the STEM mode of some nanotubes confirmed the atomic structure reported here. Owing to the difficulties explained above, electron diffraction of the isolated nanostructures could not be performed. However, fast Fourier transform analysis (FFT) was found to be of great utility here. All the FFT analyses were done with Velox (Thermo Fisher) software.

### **3. Results and discussion**

#### **3.1. XRD patterns**

**Figure S2** (SI) shows the resemblance of an XRD pattern of the reaction product to that of the pristine 2H-MoS<sub>2</sub> powder. The predominance of the (002) peak and its narrow shape indicates clearly that the 2H-MoS<sub>2</sub> flakes are at least a few nm thick. The patterns differ, however, in

some characteristic minor peaks of the  $\text{MoO}_{3-x}$  and  $\text{MoO}_2$  powder at  $\theta = 23$  and  $26.5^\circ$ , respectively (green pattern).<sup>20</sup> In addition to  $\text{MoS}_2$  reflection, ablated powder shows reflection from  $\text{Mo}_2\text{S}_3$  and sulfur, which would be expected to be formed due to the vigorous heating and rapid evaporation of  $\text{MoS}_2$ .

### 3.2. SEM-EDS analysis

SEM-EDS analysis was performed on the solar ablated product, which was found to consist mostly of  $\text{MoS}_2$  platelets with low-level carbon and oxygen contamination (5 at% each). The combination of low nanostructure yields and their small dimensions precluded systematic analysis with the present techniques, which prompted high resolution TEM analysis.

### 3.3. TEM analyses of the $\text{MoS}_2$ doublewall nanotubes

TEM analysis revealed many doublewall  $\text{MoS}_2$  tubes, a representative example of which is shown at two magnifications in **Fig. 2a** and **b**. About half of the nanotubes were open ended, suggesting that they formed rapidly (the reaction that closes the tip is likely to proceed more slowly). A few more images of such doublewall tubes are shown in **Fig. S3** (SI).

Most characteristically, the external diameter of the doublewall nanotubes varied between 6-14 nm. Their length varied between ~200-400 nm. Nevertheless, a group of short doublewall nanotubes (length <100 nm) could also be observed. In several cases, doublewall nanotubes that were cut possibly during the ultrasonic treatment were detected. **Table S1** (SI) summarizes the statistical analysis of 40 such  $\text{MoS}_2$  nanotubes. Unlike their multiwall counterparts, the layers of the doublewall nanotubes were not perfectly straight, *i.e.*, their diameter varied along their length by ~15% in most cases (**Fig. S3a** and **Table S1**). However, doublewall nanotubes with diameters varying by up to 46% were also observed in several cases. Often, though, they were buried in a chunk of ablated  $\text{MoS}_2$ , or simply covered by a  $\text{MoS}_2$  flake, and hence could not be discerned at full scale. This precluded a detailed chemical or structural analysis. The small yield and size of the doublewall nanotubes prevented the ability to separate and isolate them, *e.g.*, *via* centrifugation or filtration which is the common procedure for multiwall nanotubes.<sup>24</sup> The convolution between the signal of the doublewall tubes and the  $\text{MoS}_2$  flakes precluded high resolution TEM and electron diffraction analyses of the doublewall tubes, thereby also excluding the possibility of Raman microscopy and optical characterization.

Even though the MoS<sub>2</sub> flake (in the background) and the doublewall nanotubes are at a different zone axis to the incoming electron beam, the FFT analysis was found to be useful for understanding the nanotube structure. FFT patterns from the region of the background flake in **Fig. 2b** (orange square) and the flake with a doublewall MoS<sub>2</sub> nanotube (yellow square) are displayed in **Fig. 2c** and **2d**, respectively. Both FFTs demonstrate the hexagonal arrangement of the atoms, akin to 2H-MoS<sub>2</sub>, and correspond to the family of (100) Bragg planes. The FFT pattern in **Fig. 2d** constitutes reflections from both the flake and the nanotube. The sharp spots correspond to the flakes (orange hexagon), and the streaky pattern refers to the doublewall nanotube (yellow hexagon). The streaky pattern is known to be the hallmark of nanotube diffraction. In addition, the (100) reflection of the nanotubes is split due to the chirality of the nanotube, and the measured chiral angle is 4°. The (002) reflection from the nanotube is clearly visible with lattice spacings of 0.67 nm (green arrows). These (002) reflections are geometry forbidden in flakes (with respect to the electron beam), and hence are absent.

No further attempts to characterize the flakes were undertaken, for reasons detailed above. It can be noted, however, that the fact that the flakes appeared to be straight and thick (multiwalled) indicates that their growth mechanism is *not* the same as that of the doublewall nanotubes. In contrast to the doublewall tubes that are formed by sulfurization of the oxide vapors, the flakes are believed to form by direct deposition of the solar ablated MoS<sub>2</sub> powder (see Eq. 1). The interlayer spacing (0.67 nm) in the nanotube is slightly larger than the interlayer spacing in the corresponding flake, *i.e.*, 0.615 nm. The detailed FFT analysis is further illustrated in **Fig. S4**. The FFT pattern of the fullerene-like portion is shown (see the inset of **Fig. S4**, #3). Two sets of (002) Bragg planes are separated by an angle of 58°, which is crystallographically equivalent to the faceting angle of the fullerene-like structure, *i.e.*, 122° (see the marked angle on the nanoparticle).

Infrequently, singlewall MoS<sub>2</sub> nanotubes were also visible, as shown in **Fig. S5**, along with multiwall MoS<sub>2</sub> nanotubes with narrow diameters (<50 nm, see for example **Fig. S6**). The FFT image was taken from the tip of the singlewall nanotube, which protruded out of the flake. It shows a hexagonal pattern corresponding to the (100) Bragg planes of the nanotube. Since the nanotube is singlewalled, the (002) spots were, as expected, absent from the diffractogram. The fact that singlewall nanotubes were rare compared to the doublewall nanotubes is probably related to the stable 2H structure, which consists of two MoS<sub>2</sub> planes with hexagonal symmetry. However, given the different number of atoms in the outer and

inner walls of the nanotube, full commensuration between the two walls of a doublewall tube is not possible, and is preserved only locally.

Several triplewall nanotubes were observed (**Fig. S7**). Their walls are far flatter than those of their doublewall counterparts. Their scarceness reinforces the prediction of our molecular dynamics simulations (Section 4) that the corrugation of nanotube walls at elevated temperature favors the abundance of *doublewall* nanotubes. Furthermore, the smoothness of their walls reflects the fact that the interlayer van der Waals forces stabilize the surface charge leading to the walls of *multiwall* nanotubes being straight rather than corrugated.

**Figure S6c** shows the electron diffraction of the multiwall nanotube shown in **Fig. S6b**. Its growth axis is represented by the purple double arrow. There are 12 spots corresponding to two sets of hexagonal (100) Bragg planes. The splitting here is likely due to the rotation of the nanotube layers with respect to each other by approximately  $30^\circ$ .

Hollow closed-cage few- and multiwall MoS<sub>2</sub> nanostructures were also found in the ablated powder. **Figure S8** displays two of them. While the multiwall nanostructures were mostly faceted, the few-wall nanoparticles were more rounded (*vide infra*). One can see here that MoS<sub>2</sub> shows similar behavior to the rings of doublewall carbon nanotube bundles.<sup>25</sup> This would imply that the formation mechanism for these nanostructures may involve a balance between tube-to-tube van der Waals adhesion and the strain energy induced by local curvature.

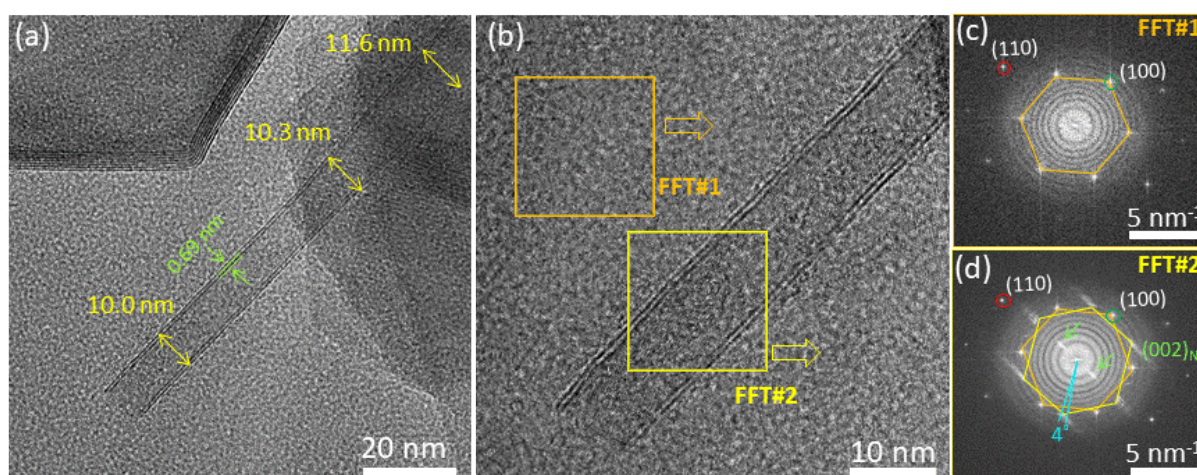


**Figure 2.** (a) TEM image of an individual doublewall MoS<sub>2</sub> nanotube which is part of a fullerene-like structure. The flakes in the background are clearly visible. (b) A further

magnified image shows the open-ended structure of a doublewall nanotube. (c and d) FFT images collected from the image (b). The FFTs are collected separately from the (c) flat flake and (d) nanotube (on top of the flake). The spots from the nanotube and the background flake are clearly distinguishable. The FFT in (d) shows the streaky hexagonal pattern (yellow hexagon) of the doublewall MoS<sub>2</sub> nanotube and six pairs of sharp spots (on the orange hexagon) corresponding to the underlying MoS<sub>2</sub> flakes. (100)  $d = 0.27$  nm and (110)  $d = 0.16$  nm. NT denotes nanotube.

### 3.4. STEM-EDS and HAADF analyses

STEM-EDS and HAADF analyses of a representative doublewall nanotube are shown in **Fig. 3**. The TEM and HAADF analysis (**Fig. 3a** and **3b**) clearly shows its contour. The STEM-EDS analysis shows that it consists of pure molybdenum and sulfur atoms. Quantitative analysis of its content revealed an S/Mo atomic ratio  $\sim 2:1$ . In addition, oxygen and nitrogen were distributed homogeneously, suggesting that they belong to the background.

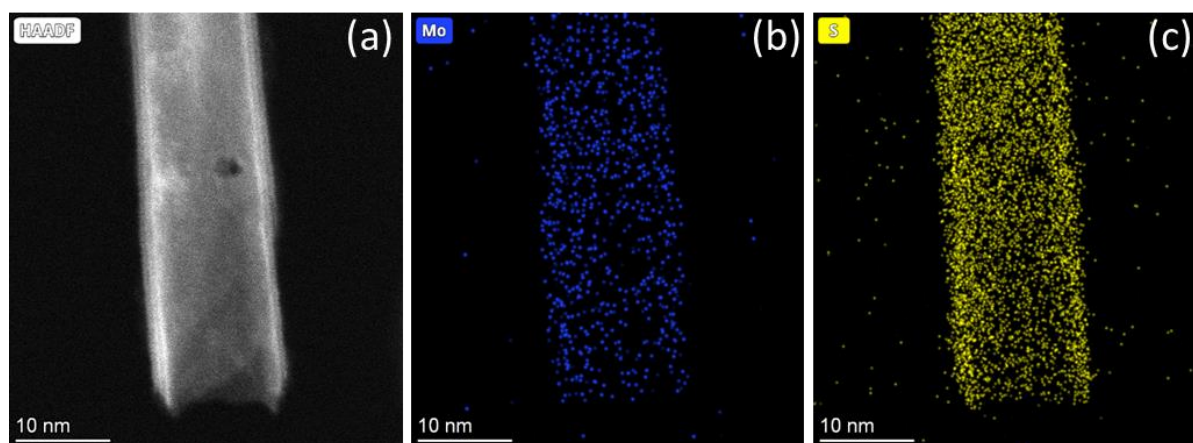


**Figure 3.** STEM-EDS and HAADF analysis of a typical doublewall MoS<sub>2</sub> nanotube.

While the singlewall closed-cage nanoparticles were mostly quasi-spherical, their multiwall counterparts were more faceted with an overall polyhedral shape that included sharp corners and cusps. Theoretical analysis of the elastic energy of folding of such nanoparticles has been presented, showing that the formation of cusps becomes more favorable the larger the ratio of the thickness of the MoS<sub>2</sub> layers to the radius of the nanoparticles.<sup>26</sup>

### 3.5. MoS<sub>2</sub> nanocones(horns)

MoS<sub>2</sub> nanohorns can have one or two squares at their apex. Unfortunately, in the latter case, line defects and other dislocations induce much more complex structure for the MoS<sub>2</sub> nanohorns, as explained below. **Figure 4** displays a multiwall MoS<sub>2</sub> nanocone (nanohorn) and a doublewall nanohorn in the bottom right. **Figure S9** shows HAADF (a) and TEM (b) micrographs of two additional multiwall nanohorns of similar morphology. Since the contrast is sharper for the multiwall nanohorn and the FFT analysis is clearer, the analysis below was carried out on the multiwall nanohorn. Tilting the nanohorn at different angles (0-40°) shows that its overall shape was preserved. To the right of the multiwall nanohorn, a doublewall nanocone is evident which also conserves its overall shape upon tilting. The inner layers of the multiwall nanocone tilted at 20° (b) and 40° (d) seem to end in a sharp tip, while the outer layers fold smoothly with no acute-angle cusps, indicating that the MoS<sub>2</sub> layer can fold to acute angles continuously without being damaged. **Figure S10a** displays a doublewall nanohorn terminating at an acute angle. The fact that the MoS<sub>2</sub> layer can fold with such a sharp angle continuously is rather surprising and calls for future detailed calculations of such unique structures. The FFT patterns in **Fig. 4d-f** were collected from the multiwall nanohorn shown in **Fig. 4a-c**, respectively. The nanohorn is placed on the MoS<sub>2</sub> flake and the FFTs in **Fig. 4d-f** consist of the FFTs of the two kinds of MoS<sub>2</sub> morphologies. For reference purposes, the FFT image from the underside of the MoS<sub>2</sub> flake is shown in the inset of the respective images (**Fig. 4a-c**). The FFT pattern of the nanowall (without any tilting, **Fig. 4a**) shows two sets of hexagonal spots that are rotated by 30° with respect to each other. These spots show two-fold rotations and are assigned to the (100) plane.

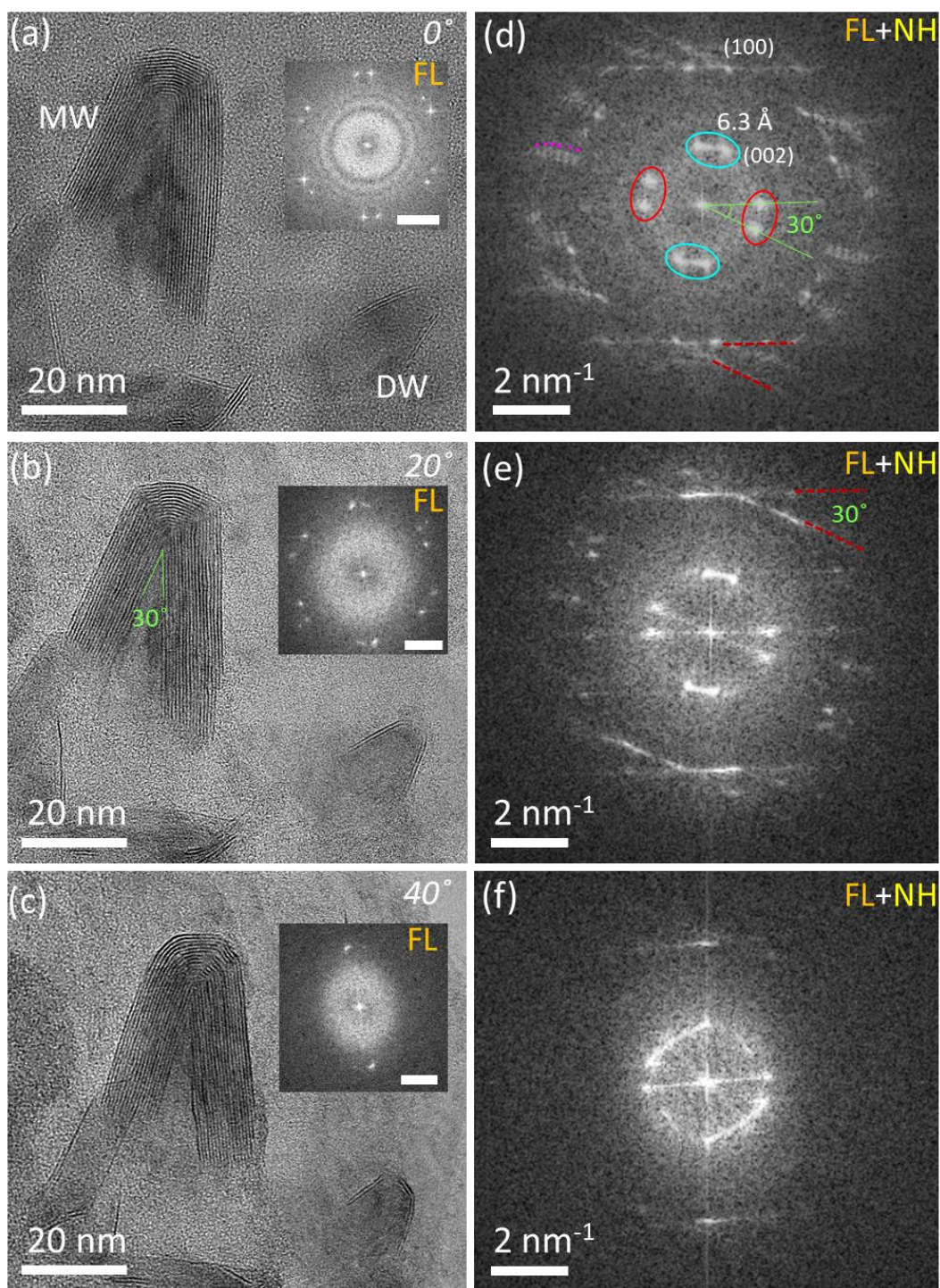


**Figure 4.** TEM images of multiwalled and doublewalled nanohorns of MoS<sub>2</sub> tilted at (a) 0°, (b) 20° and (c) 40°. The FFT pattern in the inset of the image is collected from the flakes in the background. (d-f) The FFT pattern collected from the multiwall nanohorn region. The spots identified in the red ellipse correspond to the sidewalls of the nanohorn and are rotated by 30°. The spots identified in the cyan ellipse are perpendicular to the one in the red ellipse and correspond to the apex layers of the nanohorn. The Bragg planes (100) and (002) are marked by measuring the interplanar spacings. NH and FL stand for nanohorn and flakes,

respectively. MW and DW denote multiwall and doublewall, respectively. The purple spots adjacent to the (100) diffractions in (d) reflect the conical shape of the multiwall nanohorn.

### 3.6. Bragg planes of the MoS<sub>2</sub> nanohorn

In **Fig. 4d**, a series of (100) spots (hexagonal symmetry) appear to be very different from those of the nanotube as well as the flakes. Instead of a streaked (nanotube)/sharp (flake) pattern, a faint but distinguishable series of spots going outwards can be discerned (up to six such distinguishable spots can be counted as indicated by the purple dots, see **Fig. 4d**). This series is the hallmark of the conical shape of the walls, each with a different diameter. The appearance of two sets of (002) planes in the nanohorn was not seen in the case of nanotubes. The analysis shows that the two pair spots marked by the red ellipse belong to the side walls of the nanohorn and are separated by 30°. The independent FFT analysis of left and right side walls (not shown here) infers that one spot inside the ellipse corresponds to the left-hand walls and the other is diffracted from the right-hand side walls. These results also confirm that the left and right-hand side walls of the multiwall nanohorn are tilted by 30° with respect to each other. Similarly, the discrete FFT analysis of the apex walls of the nanohorn reveals that the (002) spots marked in the cyan ellipse originate from the apex of the nanohorn, and are perpendicular to the diffraction from the sidewalls. Here too, the (002) spots were split into two due to the twofold rotation in these layers. As the nanohorn is tilted by 20° and 40° (**Fig. 4e** and **4f**), the intensity of the (100) spots of the nanohorns diminishes and the (002) planes intensify. This effect may be due to the (100) plane moving away from the diffraction zone. At a 40° tilt (**Fig. 4f**), only two (100) spots in the direction of the cone are visible, along with intense (002) planes. The FFT analysis confirms that the observed nanohorn structure is unique and different from nanotubes and nanoscrolls.

### 3.7. Partial scrolling of few-layer MoS<sub>2</sub> flakes

Another generic form of the ablated MoS<sub>2</sub>, nanoscrolls, is shown in **Fig. S10b**. Seemingly, two edges of the triangular-shaped thin MoS<sub>2</sub> flake started to roll in on themselves, forming nanoscrolls at each of the two edges. This form indicates that the heated thin triangular MoS<sub>2</sub> flake softens and becomes flexible, lowering its scrolling energy. The extra energy gained by the van der Waals interaction between the walls of the nanoscroll grant extra stability to these triangular structures. The rapid cooling rate of the ablated material limits the degree of folding of the nanoscroll edges to a diameter of only a few nm on each side of the MoS<sub>2</sub> triangular sheet. MoS<sub>2</sub> nanoscrolls have been described in the literature.<sup>27,28</sup> Nonetheless it is equivocal

to draw conclusions about the present scrolling process from the previous publications, due to the largely different synthetic conditions.<sup>27,29</sup>

**Figure S11** reveals two unique hollow-cage nanostructures observed here. **Figure S11(a)** displays a doublewall triangular MoS<sub>2</sub> nanostructure that is probably a 2D projection of a tetrahedron made of four triangles symmetrically located at the vertices of the honeycomb MoS<sub>2</sub> lattice.<sup>30</sup> The precise structure of such tetrahedra remains to be elucidated. **Figure S11b** displays the 2D projection of a multiwall nanooctahedron made of six rhombi symmetrically situated at the vertices of the honeycomb MoS<sub>2</sub> lattice. This nanostructure has been documented previously.<sup>17-19</sup> It is striking that, in agreement with a previous work,<sup>19</sup> the inner MoS<sub>2</sub> walls of this nanooctahedron comprise sharp cusps whereas the outermost layers accommodate a far more rounded shape.

#### 4. Molecular dynamics simulations

Molecular dynamics (MD) simulations in an isothermal–isobaric (NPT) ensemble with the QuantumATK package<sup>31,32</sup> were used to evaluate the impact of high temperature on the formation of MoS<sub>2</sub> nanostructures. Three different structures were considered: single-layer, bi-layer, and multi-layer (eight layers) of the 2H-phase of MoS<sub>2</sub> as taken from the Materials Project database.<sup>33</sup> Each layer was modelled as a 20×20×1 rectangular supercell. The initial vertical distance between the layers in the bi- and multi-layer configuration corresponds to the interlayer distance of the bulk (0.615 nm). Periodic boundary conditions in all directions were imposed for all simulations.

A vacuum layer of 3.0 nm was added to the direction orthogonal to the layers to avoid interaction from adjacent periodic images. A reactive force-field (ReaxFF) interatomic potential was used for Mo and S to study movements, energetics and forces in MoS<sub>2</sub>.<sup>34</sup> 5000 fs MD simulations were run at 800°C, 1 bar, and a time step of 1 fs. The results were analyzed using the Atomistic Simulation Environment (ASE) package.<sup>35</sup>

The equilibrium structures of mono-, bi- and multilayer MoS<sub>2</sub> after annealing at 800 °C at the end of 5000 fs are shown in **Fig. 5**, illustrating a significant corrugation of the layers in the mono- and bi-layer structures, which almost disappears in the multilayered structure.

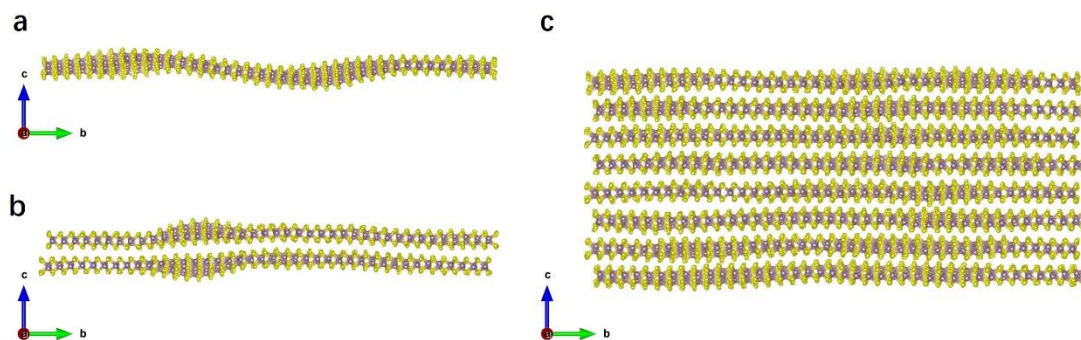


**Figure 5.** Snapshots of computed equilibrium structures of mono-, bi- and multilayer MoS<sub>2</sub> after annealing at 800°C at the end of 5000 fs by molecular dynamics simulations. The yellow and purple spheres represent the S and Mo atoms, respectively.

The variance of the vertical displacements (*c*-direction) in the Mo atoms is 0.14 nm, 0.087 nm and 0.044 nm for the mono-, bi-, and multilayers, respectively. Assuming that the nanotubes form *via* layer-by-layer deposition, the high degree of corrugation in the mono- and bilayer cases establishes a kind of kinetic barrier to the growth of multiwall nanotubes. Given the rapid cooling rate of the vaporized MoS<sub>2</sub>, this kinetic barrier can partially explain the preferred occurrence of the double layer nanotubes. In fact, careful analysis of the product revealed only small amounts of singlewall nanotubes, and even then with problematic reproducibility. This stands in contrast to the repeatable observation of numerous corrugated doublewall nanotubes in most experiments. Multiwall nanotubes with straight layers were abundant. The stability of the doublewall nanotubes can be attributed to the 2H polytype structure of MoS<sub>2</sub>, which is preserved locally in the nanotubes.

## 5. Conclusions

The experimental realization of a panorama of fundamentally small MoS<sub>2</sub> nanostructures, subsuming single- and doublewall nanotubes along with ultrasmall nanohorns and nanocones has been presented. They were all generated in solar ablation experiments conducted in a solar furnace at ultrahigh irradiance, where the precursor powder mixture comprised MoS<sub>2</sub>+MoO<sub>3</sub>. Extensive characterization of the products was performed with TEM, ED, SAED, XRD, STEM-EDS and HAADF.

Toward a better understanding of the predominant appearance of doublewall MoS<sub>2</sub> nanotubes and nano-horns, molecular dynamics simulations were conducted. They revealed how the corrugation of MoS<sub>2</sub> layers, which can occur as a consequence of large thermal fluctuations at

the high temperatures produced far from equilibrium in the solar reactor, favor these nanostructures relative to the bulk material. These calculations also show why there should be a large variance in the diameter of the doublewall tubes, in agreement with experimental results.

The presence of  $\text{MoO}_3$  in the precursor mixture appears to be crucial (*e.g.*, Eq. (1)) along with an apparent catalytic value that helps to overcome substantial kinetic barriers, such that the products and their frequency of occurrence better reflect thermodynamic stability criteria. The present method for generating  $\text{MoS}_2$  nanoparticles uses exclusively safe solid precursors, in contrast to established methods that require hazardous or toxic gaseous precursors such as  $\text{H}_2$  and  $\text{H}_2\text{S}$ , thereby creating safer reactor conditions amenable to industrial scale-up.

Notwithstanding substantial difficulties for the high-yield mass production of all these singular fundamentally small  $\text{MoS}_2$  nanoparticles, the above experimental and theoretical results motivate further research in this direction. Part of the difficulty is that solar ablation (or, for that matter, laser or arc-discharge ablation) leads to a noticeable loss of stoichiometry by breaking the more fragile Mo-S bonds, thereby vaporizing sulfur. Furthermore, in the absence of any catalyst, the poor electrical and thermal conductivity of the precursor pellet makes its ablation even harder. In the experiments reported here, it would appear that insufficient heat dissipation and temperature gradients in the ablated pellet lead to a violation of the stoichiometry of the  $\text{MoS}_2$  that is conducive to alternative chemical pathways. Possibly, corrective elements such as using a metal catalyst, *e.g.*, early transition metals (Co, Ni, Mn), soft metals (Pb, Bi) or coinage metals (Au, Pt, Pd), could make the difference. Also, a partial pressure of the sulfur vapor in the ablation zone might be able to prevent the stoichiometric imbalance. More work is needed in this direction in order to demonstrate a reliable route for the high-yield production of singular  $\text{MoS}_2$  nanostructures such as single and doublewall nanotubes and nanooctahedra.

### **Supporting Information**

Supporting Information is available from the Wiley Online Library or from the author.

### **Acknowledgements**

We are grateful to Dr. Y. Feldman for the XRD analysis. This research was supported by Grant 7130970101 (339/18) from the Israel Science Foundation. The support of the Irving and

Cherna Moskowitz Center for Nano and Bio-Nano Imaging, the Perlman Family Foundation, the Kimmel Center for Nanoscale Science (Grant 43535000350000), and the programme investissement d'avenir (investments for the future) of the "Agence Nationale de la Recherche" (National Agency for Research of France) under award number ANR-10-LBX-22-01-SOLSTICE, are gratefully acknowledged. K.Z. acknowledges a research fellowship from China Scholarship Council Grant no. 2020008500162

Received: ((will be filled in by the editorial staff))

Revised: ((will be filled in by the editorial staff))

Published online: ((will be filled in by the editorial staff))

## References

- [1] T. Barbe, G. Flamant, E. Nadal, A. Vossier, G. Olalde, J.M. Gordon, F. Bataille. Elucidating the gas flow dynamics in a nanomaterial synthesis solar reactor, *Chem. Eng. J.* 442, 135846 (2022).
- [2] R.R. Chianelli, E.G. Prestridge, T.A. Pecorano, J.P. DeNeufville. Molybdenum disulfide in the poorly crystalline 'rag' structure, *Science* 203, 1105–1107 (1979).
- [3] R. Tenne, L. Margulis, M. Genut, G. Hodes. Polyhedral and cylindrical structures of tungsten disulphide, *Nature* 360, 444–446 (1992).
- [4] Y. Feldman, E. Wasserman, D.J. Srolovitz, R. Tenne. High rate, gas phase growth of MoS<sub>2</sub> nested inorganic fullerenes and nanotubes, *Science* 267, 222–225 (1995).
- [5] S. Iijima, T. Ichihashi. Single-shell carbon nanotubes of 1-nm diameter, *Nature* 363, 603-605 (1993).
- [6] P. Nikolaev, M.J. Bronikowski, R.K. Bradley, F. Rohmund, D.T. Colbert, K.A. Smith and R.E. Smalley, Gas-phase catalytic growth of single-walled carbon nanotubes from carbon monoxide, *Chem. Phys. Lett.* 313, 91-97 (1999).
- [7] A. Loiseau, F. Willaime, N. Demoncey, G. Hug, H. Pascard. Boron nitride nanotubes with reduced numbers of layers synthesized by arc discharge, *Phys. Rev. Lett.* 76, 4737-4740 (1996).
- [8] M. Liu, K. Hisama, Y. Zheng, M. Maruyama, S. Seo, A. Anisimov, T. Inoue, E.I. Kauppinen, S. Okada, S. Chiashi, R. Xiang, S. Maruyama. Photoluminescence from single-walled MoS<sub>2</sub> nanotubes coaxially grown on boron nitride nanotubes. *ACS Nano* 15, 8418–8426 (2021).
- [9] V. Brüser, R. Popovitz-Biro, A. Albu-Yaron, T. Lorenz, G. Seifert, R. Tenne, A. Zak. Single- to triple-wall WS<sub>2</sub> nanotubes obtained by high-power plasma ablation of WS<sub>2</sub> multiwall nanotubes, *Inorganics* 2, 177-190 (2014).

- [10] T. Lorenz, D. Teich, J.-O. Joswig, G. Seifert. Theoretical study of the mechanical behavior of individual TiS<sub>2</sub> and MoS<sub>2</sub> nanotubes, *J. Phys. Chem. C* 116, 11714–11721 (2012).
- [11] J.D. Cain, F. Shi, J. Wu, V.P. Dravid. Growth mechanism of transition metal dichalcogenide monolayers: The role of self-seeding fullerene nuclei, *ACS Nano* 10, 5440–5445 (2016).
- [12] A. Patsha, V. Sheff, A. Ismach. Seeded-growth of WS<sub>2</sub> atomic layers: the effect on chemical and optical properties, *Nanoscale* 11, 22493 (2019).
- [13] H.R. Gutiérrez, N. Perea-López, A. Laura Elías, A. Berkdemir, B. Wang, R. Lv, F. López-Urías, V.H. Crespi, H. Terrones, M. Terrones. Extraordinary room-temperature photoluminescence in triangular WS<sub>2</sub> monolayers, *Nano Lett.* 13, 3447–3454 (2013).
- [14] N. Karousis, I. Suarez-Martinez, C.P. Ewels, N. Tagmatarchis. Structure, properties, functionalization, and applications of carbon nanohorns, *Chem. Rev.* 116, 4850–4883 (2016).
- [15] N. Arora, N.N. Sharma. Arc discharge synthesis of carbon nanotubes: Comprehensive review, *Diamond & Related Materials* 50, 135–150 (2014).
- [16] C. Journet, M. Picher, V. Jourdain. Carbon nanotube synthesis: from large-scale production to atom-by-atom growth, *Nanotechnology* 23, 142001 (2012).
- [17] P.A. Parilla, A.C. Dillon, K.M. Jones, G. Riker, D.L. Schulz, D.S. Ginley, M.J. Heben. The first true inorganic fullerenes? *Nature* 397, 114 (1999).
- [18] A.N. Enyashin, S. Gemming, M. Bar-Sadan, R. Popovitz-Biro, S.Y. Hong, Y. Prior, R. Tenne, G. Seifert. Structure and stability of molybdenum sulfide fullerenes, *Angew. Chem. Int. Ed.* 46, 623-627 (2007).
- [19] A. Albu-Yaron, M. Levy, R. Tenne, R. Popovitz-Biro, M. Weidenbach, M. Bar-Sadan, L. Houben, A.N. Enyashin, G. Seifert, D. Feuermann, E.A. Katz, J.M. Gordon. MoS<sub>2</sub> hybrid nanostructures: From octahedral to quasi-spherical shells within individual nanoparticles, *Angew. Chem. Int. Ed.* 50, 1810-1814 (2011).
- [20] P.E. Blackburn, M. Hoch, H.L. Johnston. The vaporization of molybdenum and tungsten oxides, *J. Phys. Chem.* 62, 769-773 (1957).
- [21] (a) T. Ressler, R.E. Jentoft, J. Wienold, M.M. Günter, O. Timpe. In situ XAS and XRD studies on the formation of Mo suboxides during reduction of MoO<sub>3</sub>, *J. Phys. Chem. B* 104, 6360-6370 (2000); (b) T. Ressler, J. Wienold, R.E. Jentoft. Formation of bronzes during temperature-programmed reduction of MoO<sub>3</sub> with hydrogen—an in situ XRD and XAFS study, *Solid State Ionics* 141–142, 243–251 (2001).
- [22] P. Chithaiah, S. Ghosh, A. Idelevich, L. Rovinsky, T. Livneh, A. Zak. Solving the “MoS<sub>2</sub> nanotubes” synthetic enigma and elucidating the route for their catalyst-free and scalable production, *ACS Nano* 14, 3004–3016 (2020).

- [23] New High-Temperature Pb-Catalyzed Synthesis of Inorganic Nanotubes, O. Brontvein, D.G. Stroppa, R. Popovitz-Biro, A. Albu-Yaron, M. Levy, D. Feuerman, L. Houben, R. Tenne and J.M. Gordon, *J. Am. Chem. Soc.* 2012, 134, 16379–16386.
- [24] Y. Yomogida, Z. Liu, Y. Ichinose, K. Yanagi. Sorting transition-metal dichalcogenide nanotubes by centrifugation, *ACS Omega* 3, 8932-8936 (2018).
- [25] J.-F. Colomer, L. Henrard, E. Flahaut, G. Van Tendeloo, A.A. Lucas, Ph. Lambin. Rings of double-walled carbon nanotube bundles, *Nano Letters* 3, 685-689 (2003).
- [26] D.J. Srolovitz, S.A. Safran, R. Tenne. Elastic equilibrium of curved thin films, *Phys. Rev. B* 49, 5260-5270 (1994).
- [27] Z. Wang, H.-H. Wu, Q. Li, F. Besenbacher, X.C. Zeng, M. Dong. Self-scrolling MoS<sub>2</sub> metallic wires, *Nanoscale* 10, 18178-18185 (2018).
- [28] J. Meng, G. Wang, X. Li, X. Lu, J. Zhang, H. Yu, W. Chen, L. Du, M. Liao, J. Zhao, P. Chen, J. Zhu, X. Bai, D. Shi, G. Zhang. Rolling up a monolayer MoS<sub>2</sub> sheet, *Small* 12, 3770–3774 (2016).
- [29] N. Karousis, I. Suarez-Martinez, C.P. Ewels and N. Tagmatarchis, Structure, properties, functionalization, and applications of carbon nanohorns, *Chem. Rev.* 116, 4850–4883(2016).
- [30] L. Margulis, G. Salitra, R. Tenne and M. Talianker, Nested fullerene-like structures, *Nature* 365, 113-114 (1993).
- [31] D.J. Evans, G.P. Morriss. The isothermal/isobaric molecular dynamics ensemble, *Phys. Lett. A* 98, 433-436 (1983).
- [32] S. Smidstrup, T. Markussen, P. Vancraeyveld, J. Wellendorff, J. Schneider, T. Gunst, B. Verstichel, D. Stradi, P.A Khomyakov, U.G. Vej-Hansen. QuantumATK: an integrated platform of electronic and atomic-scale modelling tools, *J. Phys.: Cond. Matter* 32, 015901 (2019).
- [33] A. Jain, S.P. Ong, G. Hautier, W. Chen, W.D. Richards, S. Dacek, S. Cholia, D. Gunter, D. Skinner, G. Ceder, K.A. Persson. Commentary: The materials project: A materials genome approach to accelerating materials innovation, *APL Materials* 1, 011002 (2013).
- [34] A. Ostadhosseini, A. Rahnamoun, Y. Wang, P. Zhao, S. Zhang, V.H. Crespi, A.C.T. van Duin. ReaxFF reactive force-field study of molybdenum disulfide (MoS<sub>2</sub>), *J. Phys. Chem. Lett.* 8, 631-640 (2017).
- [35] L.A. Hjorth, M.J. Jørgen, J. Blomqvist, I.E. Castelli, R. Christensen, M. Dułak, J. Friis, M.N. Groves, B. Hammer, C. Hargus, E.D. Hermes, P.C. Jennings, J.P. Bjerre, J. Kermode, J.R. Kitchin, K.E. Leonhard, J. Kubal, K. Kaasbjerg, S. Lysgaard, M.J. Bergmann, K.W. Jacobsen. The atomic simulation environment-a Python library for working with atoms, *J. Phys.: Condens. Matter* 29, 273002 (2017)